11-10-2016

Designing a Continuously Variable Magnetic Gear

J. Pritchard
University of North Carolina at Charlotte

Pavithra Padmanathan
University of North Carolina at Charlotte

Jonathan Z. Bird
Portland State University, bird@pdx.edu

Designing a Continuously Variable Magnetic Gear

J. Pritchard*, P. Padmanathan* J. Z. Bird*,†

*Electrical and Computer Engineering Department
University of North Carolina at Charlotte
9201 University City Boulevard
Charlotte, NC, 28223, United States
jfpritch@uncc.edu

†Laboratory for Electromechanical Energy Conversion and Control
Portland State University
1900 SW 4th Avenue, Suite 20-13
Portland, OR, 97201
jonathan.bird@ieee.org

Keywords: flux focusing, magnetic gearbox, torque ripple, harmonic analysis.

Abstract

This paper investigates the performance capabilities of a continuously variable magnetic gearbox that utilizes a flux focusing rotor structure. A fractional slot stator winding is designed to couple to the outer rotor of an existing magnetic gearbox in order to enable the magnetic gearbox to operate with a variable gear ratio.

1. Introduction

A coaxial magnetic gear (MG) enables speed amplification without mechanical contact. MGs do not require gear lubrication, they have inherent overload protection and they have the potential for quiet operation and high conversion efficiency [1-4]. The flux-focusing coaxial MG, as shown in Figure 1 , consists of an inner rotor with p_h pole-pairs, an outer rotor with p_c pole-pairs and a central rotor made of n_l ferromagnetic segments. The governing equation for a coaxial MG is [1]

$$\omega_h p_h = n_l \omega_l - p_c \omega_c \qquad (1)$$

where ω_h = high-speed angular velocity (on rotor 1), ω_l = low-speed angular velocity (on rotor 2) and ω_c is often stationary (ω_c=0 on rotor 3). Shah [5] demonstrated that if the input speed varies the output speed can be made constant using a separate external motor to drive the outer rotor. This results in a continuously variable magnetic gear (CVMG) with a gear ratio given by:

$$G_r = \frac{\omega_h}{\omega_l} = \frac{n_l}{p_h} - \frac{p_c}{p_h}\frac{\omega_c}{\omega_l} \qquad (2)$$

when $\omega_c = 0$, $G_r = n_l/p_h$, which is the nominal gear ratio. Jian demonstrated that the same type of CVMG can be created using an outer control rotor stator [6]. Using finite element analysis (FEA), Jian simulated the performance of a 2.6:1 nominal gear ratio CVMG that used a dual Halbach rotor structure. The calculated torque and torque density were reported to be 816Nm and 136.6Nm/L respectively, but there were no experimental results to validate the calculations.
Atallah designed and tested an experimental CVMG with a 1.23:1 nominal gear ratio using a stator that interacted with an

outer control rotor [7, 8]. Using FEA, Atallah calculated a torque density of 37.8Nm/L, while the measured torque density of the experimental CVMG was 26.4Nm/L [8].

Zaini [9] and Padmanathan [10] demonstrated that a CVMG could also be created by replacing the outer rotor with a stator. However, as the stator provides a significant portion of the magnetizing flux the torque density is inherently low [11, 12], with Zaini reporting a torque density of 13.2 Nm/L. The use of the stator to magnetize the MG also significantly lowers the power factor and creates a large torque ripple [11].

In this paper a 4.25:1 nominal gear ratio CVMG with a flux focusing control rotor is investigated. The design is shown in Figure 2. Unlike other proposed topologies [6-8] the outer MG rotor, called the control rotor in this paper, shares the magnetic flux with both the stator and the inner MG rotors. As the stator interacts with the outer rotor, rather than the inner rotor, as in [7, 8] the stator torque production is more directly connected. However the disadvantage of this approach is that the required stator torque will be higher than what is needed to interact with the higher speed inner rotor.

If a CVMG can be shown to operate at high torque, relative to both the overall size and the weight of the magnets used, then it could have significant practical potential, particularly for hybrid electric vehicles [6, 8] as well as wind [8, 9] and marine hydrokinetic power generation [13]
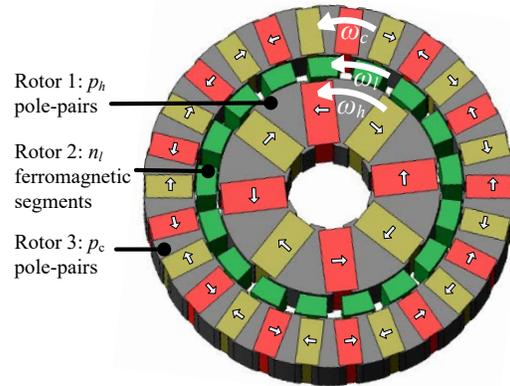

Figure 1 A coaxial magnetic gear using a flux focusing rotor topology with p_h=4 pole-pairs on the inner high-speed rotor, n_l =17 steel poles on the low-speed rotor and p_c=13 pole-pairs on the outer rotor [4].
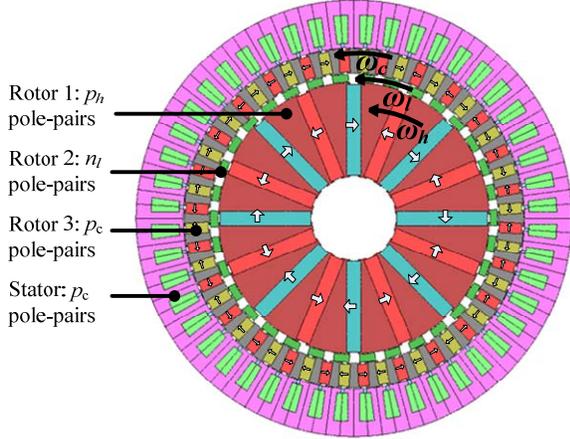
Figure 2: A flux focusing continuously variable magnetic gear with p_h=8 pole-pairs on the inner high-speed rotor, n_l =34 steel modulation poles on the low-speed rotor and p_c=26 pole-pairs on the outer control rotor. Arrows indicate magnetization direction.

2. Continuously Variable Magnetic Gear

The dominant radial field component created by the high-speed rotor (rotor 1) can be approximated by assuming that it is given by:

$$B_r^h(r,\theta,t) = b_r^h(r)\sin[p_h(\theta - \omega_h t) + p_h\theta_h] \quad (3)$$

where θ_h is the initial mechanical angular position of rotor 1. The ferromagnetic poles on rotor 2 create a radial modulating pattern with a dominant harmonic given as:

$$\Gamma_r^l(r,\theta,t) = \lambda_r^l(r)\sin[n_l(\theta - \omega_l t) + n_l\theta_l] \quad (4)$$

where θ_l is the initial mechanical angular position of rotor 2. The high-speed rotor's field modulated by rotor 2 gives a field in the outer rotor air-gap (at $r=r_c$) of:

$$B_r^c(r_c,\theta,t) = \Gamma_r^l(r_c,\theta,t)B_r^h(r_c,\theta,t) \quad (5)$$

Substituting (3) and (4) into (5) and then using a trigonometric identity one obtains:

$$B_r^c(r,\theta,t) = B_o^c\left(\cos[(n_l-p_h)(\theta - \frac{n_l\omega_l - p_h\omega_h}{n_l-p_h}t) + n_l\theta_l - p_h\theta_h] \right.$$
$$\left. - \cos[(n_l+p_h)(\theta - \frac{n_l\omega_l + p_h\omega_h}{n_l+p_h}t) + n_l\theta_l + p_h\theta_h] \right) \quad (6)$$

where $B_o^c = b_r^h(r_c)\lambda_r^l(r_c)/2$.

Assuming linearity, the torque in the control rotor's inner air-gap is [14]:

$$T = \frac{2dr_c^2}{\mu_0}\int_0^{2\pi} B_r^c(r_c,\theta,t)B_\theta^c(r_c,\theta,t)d\theta \quad (7)$$

where:

$$B_\theta^c(r_c,\theta,t) = b_\theta^c(r_c)\sin[p_c(\theta - \omega_c t) + p_c\theta_c] \quad (8)$$

is the dominant component of the radial flux density created by the outer (control) rotor and d is the axial length of the

CVMG. The integration of the two field functions in (7) will result in a non-zero torque only when

$$p_c = n_l \pm p_h. \quad (9)$$

The CVMG under study in this paper has $(p_h, p_c, n_l) = (8, 26, 34)$. Therefore

$$p_c = n_l - p_h \quad (10)$$

and so the first term in (6) applies. Given (10), for non-zero steady-state torque one must also have [15]:

$$\omega_c = \frac{n_l\omega_l - p_h\omega_h}{n_l - p_h} \quad (11)$$

with (11) the steady-state torque from (7) becomes:

$$T_c = T_o\sin(p_h\theta_h + p_c\theta_c - n_l\theta_l) \quad (12)$$

where $T_o = \frac{2dr_c^2\pi}{\mu_0}b_\theta^c(r_c)b_r^h(r_c)\lambda_r^l(r_c) \quad (13)$

is the peak torque. Substituting (10) into (11) yields (1). With $(p_h, p_c, n_l) = (8, 26, 34)$ the speed relationship in (1) is:

$$\omega_h = 4.25\omega_l - 3.25\omega_c \quad (14)$$

As the stator electrical frequency, ω_e, and mechanical angular velocity, ω_c, are related by:

$$\omega_c = \omega_e / p_c \quad (15)$$

then (14) becomes:

$$\omega_h = 4.25\omega_l - 0.125\omega_e. \quad (16)$$

Figure 3 shows geometric parameter definitions Table 1 gives the geometric parameter values, while Figure 4 shows the inner magnetic gear (MG) assembly and Figure 5 shows the assembled MG. In this paper only the stator design is being considered. The purpose of this paper is to present a stator design that can fit over a MG to enable the MG to act as a CVMG. Unlike in [16] the outer rotor, called a control rotor in this paper, is allowed to rotate and therefore will interact with both the stator winding and low speed rotor. The control rotor has p_c =26 pole-pairs and therefore a fractional slot stator winding [17], with 4/13 slots-per-pole-per-phase, has been selected so as to enable a large number of poles to be accommodated within a small relative diameter (0.226m).
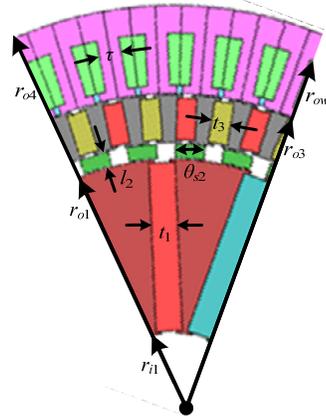

Figure 3: Definition of the geometric parameters

Description		Value	Unit
Inner rotor (high speed)	Pole pairs, p_h	8	-
	Inner radius, r_{i1}	28	mm
	Outer radius, r_{o1}	90	mm
	Magnet thickness, t_1	9.5	mm
	Airgap, g	0.5	mm
Cage rotor (low speed)	Steel poles, n_l	34	-
	Cage bar radial thickness, l_2	5	mm
	Pole span, θ_{s2}	180/p_3	degrees
Control rotor	Pole pairs, p_c	26	-
	Inner radius, r_{i3}	96	mm
	Outer radius, r_{o3}	113	mm
	Magnet thickness, t_3	7	mm
	Airgap, g	0.5	mm
Stator	Number of slots	48	-
	Tooth width, τ	8	mm
	Outer radius, r_{o4}	145	mm
	slot inner radius r_{i4}	113.5	mm
	slot outer radius, r_{ow}	135	mm
	Winding fill factor	60	%
Material	NdFeB magnet, N40H, B_r	1.25T	T
	Stator lamination steel (JFE, 35JN270)	-	-
Active region stack length, d		75	mm

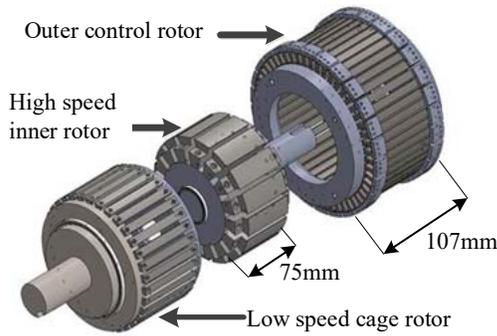Table 1: Geometric and Material Parameters

Figure 4: Exploded view of the magnetic gear mechanical assembly [16]

Figure 5: Fully assembled inner magnetic gear with outer control rotor shown [16]

The control rotor speed, ω_c, is a function of the input speed, ω_l, and the desired output speed, ω_h. When the speeds are constant the net torque on the control rotor, T_c, must be zero. The torque applied by the stator must be balanced by the torque from the MG cage rotor. A non-zero net torque can only exist during acceleration or deceleration. Therefore at steady-state the torque must satisfy

$$T_h + T_l + T_s = 0 \tag{17}$$

where T_h=high-speed rotor torque, T_l=low-speed rotor torque and T_s=stator torque.

3. Stator Harmonic Analysis

The harmonics created by the fractional slot stator winding can be investigated by computing the harmonic components. Considering the winding function [18] pattern for fractional slot phase-A winding as shown in Figure 6 the corresponding winding function for phase-A can be sketched as shown in Figure 7. The Fourier series that reproduces Figure 7 is then:

$$n(\theta) = \sum_{k=1}^{\infty} b_k \sin(k\theta) \tag{18}$$

where

$$b_k = \frac{N}{\pi k}[\cos(k\frac{9\pi}{24}) - \cos(k\frac{11\pi}{24}) + \cos(k\frac{13\pi}{24}) - \cos(k\frac{15\pi}{24})$$

$$+\cos(k\frac{35\pi}{24}) - \cos(k\frac{33\pi}{24}) + \cos(k\frac{39\pi}{24}) - \cos(k\frac{37\pi}{24}) \tag{19}$$

A plot of the winding function (18) for phase-A and the resulting 3-phase winding function is shown in Figure 8.
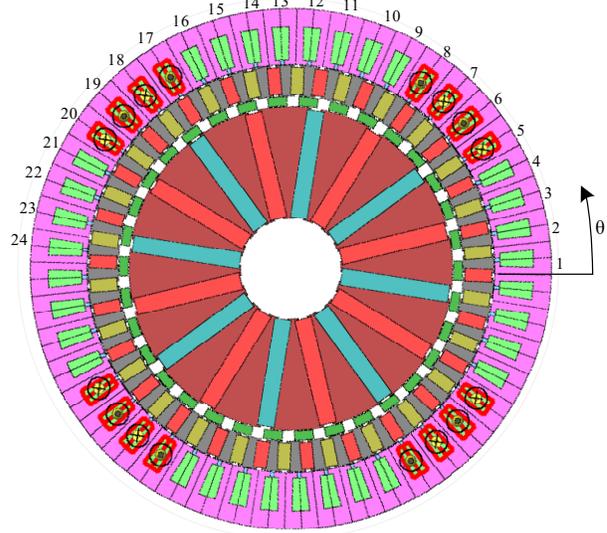

Figure 6: 48 slot stator with phase-A concentrated winding layout shown. The first 24 slot numbers are shown.
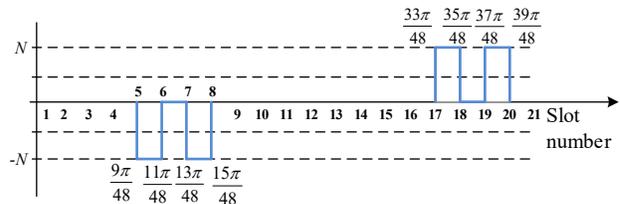

Figure 7: Winding function with corresponding slot number and angular position shown.
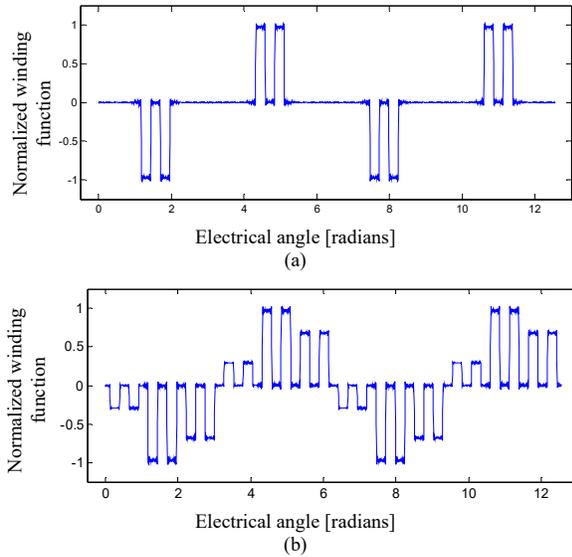
Figure 8: (a) Winding function Fourier series representation of phase A and (b) winding function for all three phases.
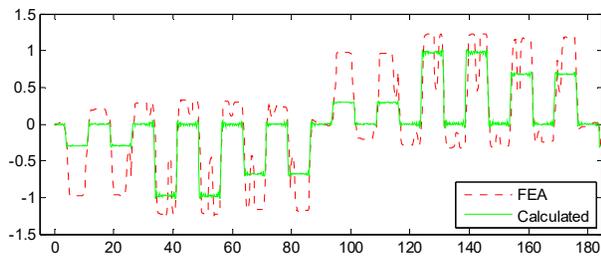

Figure 9: Overlay of analytic winding function values with the calculated magnetic flux density values [T]. The analytic values were normalized.

The harmonics created by the winding function should follow that created by the air-gap field [18]. Figure 9 compares the winding function with the radial field components computed using JMAG finite element analysis (FEA) software. FEA field values were calculated by changing the control rotor magnets to steel. This prevented any external MG harmonics from being created. Figure 9 shows that the field magnitudes are different, however the simple winding function analysis technique accurately determines the field profile. A comparison of the harmonic components calculated from the FEA and analytic model is given in Figure 10. Figure 10 confirms that the analytic model accurately predicts the presences of the relevant spatial components. A 26th harmonic component is indeed created and this is the major torque producing component.

Using the geometric and material values shown in Table 1 and electrical and mechanical values shown in Table 2 a set of magnetostatic simulations were used to calculate the torque under peak load. It was determined that the control rotor torque will go to zero when a stator current density of $J = 17$ A/mm^2 is used. A transient and magnetostatic simulation was used to confirm these results and the torque

values are shown in Table 3. The transient results show significant torque ripple. This torque ripple is not seen in simulations without stator excitation [16], which points to the stator flux harmonics as the cause.
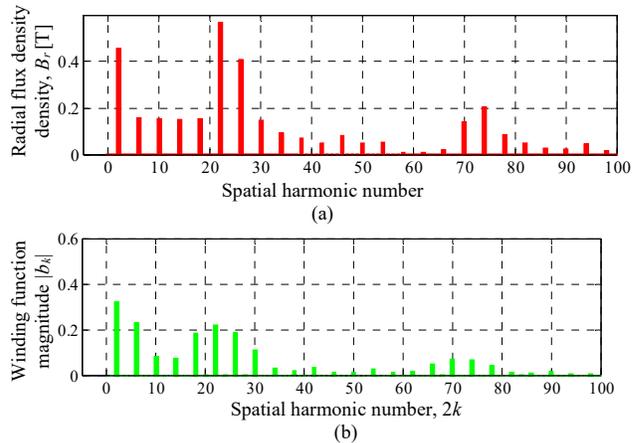

Figure 10: (a) Radial harmonic flux density calculated using FEA and (b) winding function harmonic components. The winding function analysis accuracy predicts the relevant harmonics.
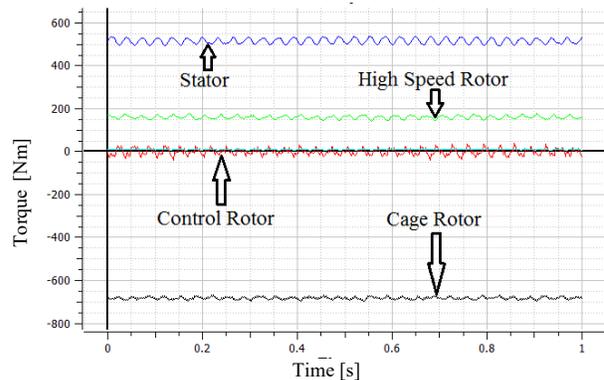

Figure 11: Transient torque analysis when the control rotor torque is made zero

Description	Value	Unit
Current amplitude, J	17	A/mm^2
Current frequency, f_e	5.2	Hz
Initial electrical angle, θ_e	25.3	degrees
High speed rotor speed, ω_h	73	rpm
Cage rotor speed, ω_l	8	rpm
Control rotor speed, ω_c	-12	rpm

Table 2: Transient simulation conditions that gives zero control rotor torque.

Component	Static [Nm]	Transient (Avg) [Nm]	Ripple [Nm]
High speed rotor	166.3	160.5	21.4
Low speed (cage) rotor	-683.9	-682.1	22.2
Control rotor	-2.0	-0.37	57.0
Stator	521.2	525.2	33.4

Table 3: Magnetostatic and transient torque calculations

4

4. Stator Design

As a current density of $J = 17 A/mm^2$ would be too high for continuous operation, when air-cooled, a parameter study was conducted in order to maximize the stator torque capability. The stator tooth width, τ, and coil outer radius, r_{ow}, were both varied while keeping the current density constant at $J = 8$ A/mm^2. The resulting stator and control rotor torques are shown in Figure 12. Figure 12(a) shows that the stator torque is maximum at τ=9.5mm. Further increases in tooth width lead to a reduction in torque. This is likely caused by flux leakage between the control rotor permanent magnets through the ends of the wider stator teeth. Further increases in the stator slot outer radius had only an incremental effect on torque, due to saturation. Figure 12(b) shows that the control rotor torque will not reduce to zero when using a $J = 8 A/mm^2$ current density. At $r_{ow} = 180$ mm the control rotor torque is still at $T_c = 28.8$ Nm. There is little improvement obtained by increasing r_{ow} further. This analysis shows that this final stator design will be too large to be constructed and will not be able to meet the peak torque operating condition of the MG (since $T_c \neq 0$).
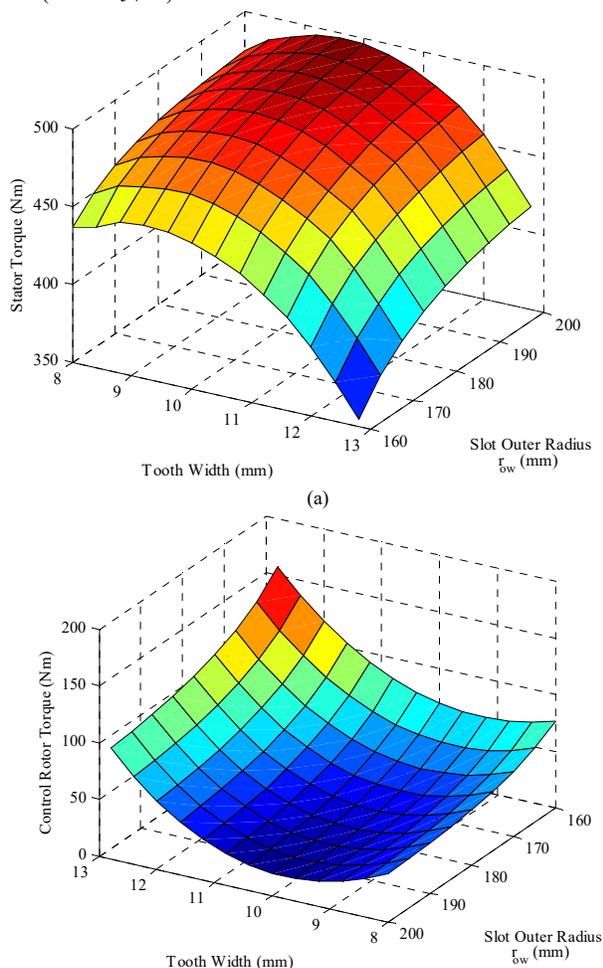

(a)

Figure 12: (a) Stator torque and (b) control rotor torque as a function of stator tooth width, τ, and stator slot outer radius, r_{ow}.

Until this point, the effective stack length of the three rotors and the stator were all assumed to be $d = 75$ mm. However in order to mechanically embed the inner rotors the outer control rotor axial length was mechanically made longer and therefore the active region of the outer rotor can accommodate additional magnets thereby enabling the outer rotor to have an axial active length of $d_s = 107$mm (refer Figure 4). As the inner rotor only has a 75mm axial active region not all of the inner rotor magnets will therefore interact with the outer control rotor magnets. If the outer stator is now designed to have a 107mm axial length it will enable a higher torque to be attained on the control rotor without significantly increasing the mechanical size of the CVMG.

The performance when using a d=75mm axial inner rotor length and a $d_s = 107$mm control rotor and stator axial length was investigated by using a 2-D simulation in which the axial length of the MG was set to 107mm and then the relative phase angle of the cage rotor torque was adjusted to reduce the MG torque down to 70% of peak value (75/107=0.7). An earlier trial had showed that increasing the magnets in one rotor alone had little effect on the maximum torque produced by the MG. Using this approach the torque analysis values shown in Table 4 were obtained when using a current density of $J = 5 A/mm^2$. The cage rotor torque is computed to be 677Nm and the control rotor torque is close to zero. This indicates that this design approach can lead to a higher torque operation at lower current density.

Component	Torque [Nm]	Torque ripple [Nm]
Low speed cage rotor	-677.1	28.7
Control rotor	-18.6	66.0
High speed rotor	158.9	29.0
Stator	539.5	35.7

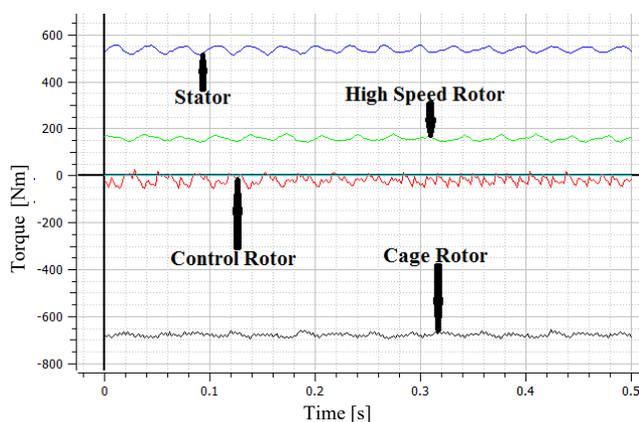Table 4: Torque and torque ripple values for $d_s = 107$mm axial stator length and $J = 5 A/mm^2$ current density.

Figure 13: Calculated transient torque for a stator stack length of d_s=107mm and $(r_{ow}, r_{o4}) = (165, 175)$ mm and $J = 5 A/mm^2$.
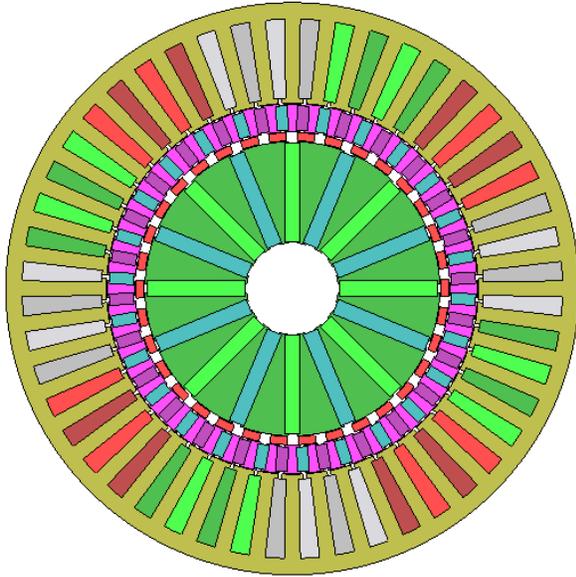
Figure 14: 2-D FEA model of the continuously variable magnetic gearbox with $(r_{ow}, r_{o4}) = (165, 175)$ mm

5. Conclusions

The initial design analysis of a flux focusing CVMG has been presented. The design differs from previous CVMG designs in that the outer rotor of the MG is used to both couple with the stator and the low-speed MG rotor. However, using this approach creates a number of challenges. In particular, the harmonics created by the stator must be carefully assessed in order to ensure that they do not create large torque ripples in the MG. Furthermore, by controlling the outer rotor of the MG the stator torque requirements are more challenging. In order to meet the MG torque requirements the active region axial length of the outer rotor of the MG and stator had to be increased.

2 Acknowledgment

References

[1] T. B. Martin, "Magnetic Transmission," USA Patent 3,378,710, 1968.

[2] P. O. Rasmussen, T. O. Andersen, F. T. Jorgensen, and O. Nielsen, "Development of a high-performance magnetic gear," *IEEE Trans. Ind. Appl.,* vol. 41, pp. 764-770, 2005.

[3] K. Atallah, S. D. Calverley, and D. Howe, "Design, analysis and realisation of a high-performance magnetic gear," *IEE Proc.-Electr. Power Appl.,* vol. 151, pp. 135-143, 2004.

[4] K. K. Uppalapati, W. Bomela, J. Bird, M. Calvin, and J. Wright, "Experimental Evaluation of Low Speed Flux Focusing Magnetic Gearboxes," *IEEE Trans. on Ind. Appl.,* vol. 50, pp. pp. 3637 – 3643, Nov/Dec 2014.

[5] L. Shah, A. Cruden, and B. W. Williams, "A variable speed magnetic gear box using contra-rotating input shafts," *IEEE Trans. Mag.,* vol. 47, pp. 431-438, 2011.

[6] L. Jian and K. T. Chau, "Design and analysis of a magnetic-geared electronic-continuously variable transmission system using finite element method," *Progr. Electrmagn. Res.,* vol. 107, pp. 47-61, 2010.

[7] J. Wang, K. Atallah, and S. D. Carvley, "A magnetic contionously variable transmission device," *IEEE Trans. Mag.,* vol. 47, pp. 2815-2818, 2011.

[8] K. Atallah, J. Wang, S. D. Calverley, and S. Duggan, "Design and Operation of a magnetic continuously variable transmission," *IEEE Trans. Ind. Appl.,* vol. 48, pp. 1288-1295, 2012.

[9] A. Zaini, N. Niguchi, and K. Hirata, "Continously variable speed vernier magnetic gear," *IEEE Trans. Mag.,* vol. 48, pp. 3104-3107, Nov. 2012.

[10] P. Padmanathan and J. Z. Bird, "A continuously variable magnetic gear," in *Electric Machines & Drives Conference (IEMDC), 2013 IEEE International*, 2013, pp. 367-373.

[11] P. Padmanathan, "Design of a continuously variable magnetic gear," M.S. Thesis, Elect. and Comp. Eng., Univ. North Carolina at Charlotte, Charlotte, USA, Dec. 2013.

[12] M. Johnson, A. Shapoury, H. A. Toliyat, P. Boghrat, and M. Post, "Review of magnetically geared motors and analysis of their potential for naval propulsion applications," presented at the Electric Machines Technology Symposium (EMTS) 2014, Villanova, PA, 2014.

[13] J. Bird, "Marine hydrokinetic power take-off using magnetic gearing," presented at the 2nd Marine Energy Technology Symposium, Seattle, WA, 2014.

[14] J. Bird, "A Decoupled Quasi-Static Stress Tensor Formulation," presented at the Advances in Magnetic Conference, Bormio, Italy, 2016.

[15] K. Atallah and D. Howe, "A Novel High-Performance Magnetic Gear," *IEEE Trans. on Magn. ,* vol. 37, pp. 2844 - 2846 2001.

[16] K. K. Uppalapati, J. Z. Bird, J. Wright, J. Pitchard, M. Calvin, and W. Williams, "A magnetic gearbox with an active region torque density of 239Nm/L," in *IEEE Energy Conv. Cong. Expo.*, 2014, pp. 1422-1428.

[17] P. Salminen, "Fractional Slot Permanent Magnet Synchronous Motors for Low Speed Applications," Ph.D. Thesis, Lappeenranta University of Technology, Lappeenranta, Finland, 2004.

[18] N. L. Schmitz and D. W. Novotny, *Introductory Electromechanics*: Ronald Press Co., 1965.